Enhancing mmWave Radar Sensing Using a Phased-MIMO Architecture

Kai Zheng
University of California San Diego
kazheng@ucsd.edu

Wuqiong Zhao
University of California San Diego
wqzhao@ucsd.edu

Timothy Woodford
University of California San Diego
twoodfor@ucsd.edu

Renjie Zhao
University of California San Diego
r2zhao@ucsd.edu

Xinyu Zhang
University of California San Diego
xyzhang@ucsd.edu

Yingbo Hua
University of California Riverside
yhua@ece.ucr.edu

ABSTRACT

Millimeter-wave (mmWave) radar has become instrumental in diverse consumer applications. Yet current radar architectures face major limitations. While full-MIMO structures are feature-rich, their cost and complexity rise rapidly with more antennas. Phased-MIMO radars promise enhanced scalability by combining large phased arrays with a small number of RF chains. Nevertheless, the phased-MIMO research thus far primarily relies on simulation or theoretical analysis. In this paper, we introduce HybRadar, a novel programmable phased-MIMO radar platform to address this experimental gap. HybRadar repurposes the phased arrays on a low-cost 802.11ad radio to create a scalable low-cost array of phased subarrays. It further incorporates transmit/receive front-end, control channel, and hardware synchronization mechanisms to enable a modular phased-MIMO system. By extending recent MIMO array synthesis models, we optimize the placement of phased subarrays to maximize the spatial resolution. Our prototype validation and case studies confirm the capability and versatility of HybRadar.

CCS CONCEPTS

• **Hardware → Sensor devices and platforms**; *Beamforming*; Digital signal processing.

KEYWORDS

mmWave radar, Sparse array, Point cloud, Compressive sensing.

ACM Reference Format:
Kai Zheng, Wuqiong Zhao, Timothy Woodford, Renjie Zhao, Xinyu Zhang, and Yingbo Hua. 2024. Enhancing mmWave Radar Sensing Using a Phased-MIMO Architecture. In *The 22nd Annual International Conference on Mobile Systems, Applications and Services (MOBISYS '24), June 3–7, 2024, Minato-ku, Tokyo, Japan.* ACM, New York, NY, USA, 14 pages. https://doi.org/10.1145/3643832.3661865

1 INTRODUCTION

For decades, millimeter-wave (mmWave) radars have played a crucial role in aviation, defense, and meteorology applications. With advances in RF hardware, they are also becoming vital in consumer-grade applications such as automotive perception [20, 45, 46, 68], wearable/mobile and contactless health monitoring [2, 17, 18, 26, 55], low-power activity and location tracking in smart spaces [84], *etc.* These applications are projected for an exponential market penetration [15]. Unlike optical sensors like cameras and LIDAR, mmWave radars maintain functionality even in adverse weather and poor lighting conditions, making them particularly attractive for emerging domains, *e.g.*, surveillance and autonomous driving.

However, consumer-grade mmWave radars currently lag behind their military-grade counterparts in spatial resolution, mostly offering only single-point ranging or tracking [24]. This roots from a combination of factors including cost, power consumption, and form-factor constraints. While the range resolution of a radar depends on its signal bandwidth which is often fixed for a given spectrum band, the angular resolution of a radar hinges upon its effective *antenna aperture* [49] which varies widely and proportionally to the number of antenna elements.

Current mmWave radars predominantly adopt a *full-MIMO* structure wherein each RF chain is singularly linked to a passive antenna. This enables flexible array processing within both the transmit path and the receive path. However, the inherent hardware complexity of the MIMO architecture hinders the scalability of the number of physical antennas. Adding an extra antenna necessitates a full RF chain, comprised of data converters, mixers, and filters, coupled with clock distribution and heat dissipation problems, among others. The cost, complexity, size, and power consumption become increasingly daunting as the system scales [52].

Phased array radars represent a contrasting approach, where multiple antennas are connected to a single RF chain through phase shifters. While more cost-effective, phased arrays only support *analog beamforming* with limited phase/amplitude resolution. It requires multiple beam scans to cover wide angles, hindering real-time operation.

In the past decade, phased-MIMO radar, also referred to as subarray MIMO radar, has been explored [21, 22, 75] to strike a balance between the above two paradigms, as illustrated in Fig. 1. The phased-MIMO radar concept was developed concurrently with the *hybrid beamforming* in communication systems [38]. Both adopt an array of subarray antenna architecture, where each RF chain can be connected to a phased array. Such subarray architecture is considered the optimal way of scaling up the number of antenna elements and hence the radar can provide close-to-LIDAR-level spatial resolution, and supreme target detectablilty, under the hardware

MOBISYS '24, June 3–7, 2024, Minato-ku, Tokyo, Japan

ACM ISBN 979-8-4007-0581-6/24/06.
https://doi.org/10.1145/3643832.3661865

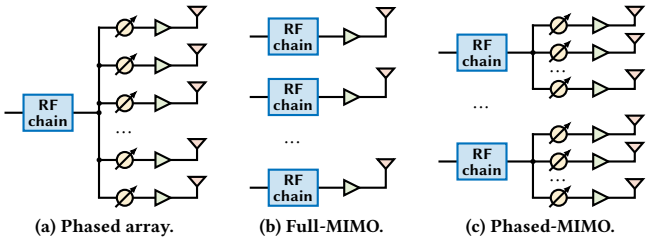

(a) Phased array. (b) Full-MIMO. (c) Phased-MIMO.

Figure 1: Radar architectures (only showing Tx).

complexity and cost constraints of commodity devices. The potential of phased-MIMO already emerged in automotive and health sensing [53, 75], and is likely to propagate to many other wireless sensing use cases such as computer-human interaction [30].

However, the degree of freedom in phased-MIMO radar sensing remains largely underexplored. Examples include waveform configuration, beam pattern (codebook) design, phased array geometry, baseband processing algorithms, *etc.* Existing work either employs numerical analysis [22] or simulation [21] which misrepresents the elusive environmental factors, or resorts to emulation using MIMO radar with a limited number of antenna elements (*e.g.*, 3×4 [75]) which underrates the scalability of phased-MIMO.

In this paper, we introduce HybRadar, a programmable phased-MIMO radar platform with a scalable array of subarray architecture. HybRadar supports digital beamforming through multiple RF chains, each of which is connected to a 32-element phased array. This design enables the platform to scale easily in multiples of 32 simply by adding more RF chains and phased arrays. More importantly, we can flexibly reconfigure the phased array beam patterns and the subarray layout, and implement any phased-MIMO baseband processing algorithms.

Inspired by the mmWave software radio in [82], we repurpose a commercial-of-the-shelf 802.11ad radio, hijack the control channel to its phased arrays, and redesign the data channel so that the phased arrays can be used to transmit/receive radar signals. We have realized both software radar that supports arbitrary radar waveform and the cost-efficient analog FMCW radar. To optimize the sensing performance of HybRadar, we make a set of design choices unique to the array of subarray setup, including *(i)* synchronization between the phased array control channel and FMCW synthesizer channel; *(ii)* designing the transmitting and receiving paths for high-frequency FMCW chirp generation and mixing; *(iii)* ensuring easy scalability towards many RF chains and antenna elements. In addition, we extend the concept of the virtual array in MIMO radar systems [49], and propose a sparse subarray layout, which achieves superior angular resolution even with a small number of phased arrays.

We have conducted comprehensive experiments to demonstrate HybRadar's capabilities and affirm the effectiveness of our design in terms of time/phase synchronization, multi-chain scalability, power budget, *etc.* Remarkably, HybRadar achieves an angular resolution of 2.46° using only 2Tx and 2Rx RF chains (64×64 antenna elements). To further illustrate the practical applications of HybRadar, we have performed two case studies: high-resolution 3D point cloud generation and compressive radar beam scanning. We first demonstrate that HybRadar can be used to generate accurate,

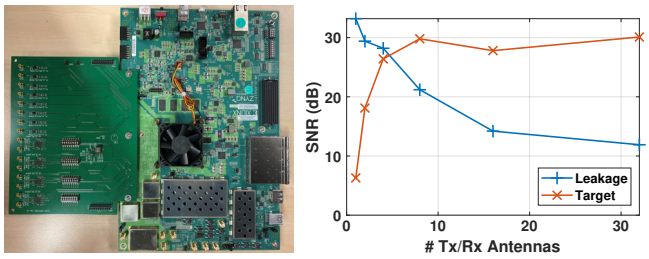

(a) RFSoC w/ the adapter board. (b) Signal and interference.

Figure 2: The implementation of digital radar.

dense 3D point clouds, similar to high-end imaging radar, even with a limited 2Tx-2Rx setup. We then design a compressive scanning codebook, which can use a small fraction of the available beams to achieve similar or even better angular accuracy than evenly spaced beam patterns.

In summary, the key contributions of this work are:

(i) The design and implementation of HybRadar, the first mmWave radar experimental platform that embodies a scalable array of subarray architecture. We intend to make HybRadar's hardware open-source and available to the research community.

(ii) The exploration of the distinctive benefits of phased-MIMO radars, particularly the development of a sparse subarray layout that delivers superior spatial resolution.

(iii) The experimental validation of HybRadar's architecture and performance, along with case studies in point cloud imaging and compressed beam scanning, demonstrating the versatility of the platform.

2 SOFTWARE DEFINED RADAR

Table 1: Digital radar vs. analog radar.

	Digital Radar	Analog Radar
Waveform Synthesis	Wideband DAC	PLL + VCO
Waveform Flexibility	Arbitrary	FMCW
Range Estimation	Digital Correlation	Analog Mixing
Baseband Bandwidth	2 GHz	10s MHz
Baseband Processing Unit	Expensive	Cheap
Extra Hardware	RFSoC Adapter Board	FMCW Front-end Board
Digital Processing	Complex	Light-weight

Our mmWave radar system is built upon the M^3 software-defined radio (SDR) platform, which modifies a COTS 802.11ad radio (Airfide Sparrow+) by integrating a custom "bridge board" for arbitrary waveform transmission.

Digital radar. Digital radar on the M^3 platform is realized by directly inputting a radar waveform into the baseband. This approach offers significant waveform design flexibility, proving crucial for various research applications, including advanced radar waveform design and the fusion of sensing with communication.

Synthesizing a wideband radar signal (4 GHz) necessitates high-end baseband processing units (BPUs) such as Xilinx RFSoC [73]. Interfacing the RFSoC with the M^3 front-end requires a specially designed adapter board. The default XM500 [74] board does not support full bandwidth across all 8 ADC/DAC channels. Therefore,

we designed a new adapter board to fully utilize all channels, shown in Fig. 2(a). We have also incorporated baseband amplifiers with adjustable gain to accommodate the wide range of radar-reflected signal strengths, ensuring compatibility with the ADCs' input range.

In our preliminary experiments using digital radar, we measure a corner reflector with a radar cross-section (RCS) of 12 dBsm at a distance of 2.5 m. We generate a −2 to 2 GHz FMCW chirp signal with a duration of 90 µs at the baseband using two DAC channels (I/Q). Subsequent Tx/Rx correlation is performed to detect the targets. Although the Tx/Rx phased array is spaced by 7 cm, we observe a strong direct-path leakage signal. However, by activating additional Tx/Rx antennas and employing beamforming, we observe a suppression of this leakage and an improvement in the SNR of the target, as shown in Fig. 2(b).

Despite its successful implementation, digital radar faces two main limitations: (i) High cost: utilizing the Xilinx RFSoC incurs a significant expense, approximately 11k USD. (ii) Complex signal processing: real-time sampling, correlation, and data management on an FPGA adds considerable complexity to system evaluation and development.

Analog radar. In contrast, the analog radar implementation replaces the "bridge board" with an "FMCW radar front-end" board, employing a voltage-controlled oscillator (VCO) and phase-locked loop (PLL) for wideband chirp signal generation. Table 1 outlines the key design differences between digital and analog radar. Given the cost-effectiveness and straightforward digital signal processing of the analog approach, the remainder of this paper will focus predominantly on the design, development, and evaluation of the analog radar system.

3 RADAR HARDWARE DESIGN

In this section, we delve into the architecture and key hardware design choices of the analog radar. The hardware is highly modular. Each module comprises 3 main components: the FMCW chirp synthesizer, the radar front-end PCB, and the phased-array module (PAM), as shown in Fig. 3(a). We have designed the synchronization mechanisms across the time, phase/frequency and control channel, so that HybRadar can scale its antenna aperture as more modules are added. Within each module, the FMCW chirp synthesizer generates a 13–17 GHz frequency sweeping signal that is connected to the radar front-end PCB. The chirp signal is subsequently upconverted into the 58–62 GHz mmWave band by the PAM originating from a COTS 802.11ad radio. The front-end PCB performs chirp signal amplification, distribution, and FMCW dechirping, and produces the beat signals that are sampled by the ADCs. The resulting baseband signals can be processed in real-time using an FPGA-based BPU (such as USRP [14] or RFSoC [73]).

3.1 Phased Array Module

We retrofit the PAM from a COTS 802.11ad radio (Airfide Sparrow+[1]) and design the control/data interfaces to repurpose it for our phased-MIMO radar. Each of the phased arrays follows a 6×6 uniform planar array (UPA) layout with 4 inactive corner elements. The beamformer inside the PAM provides 2-bit phase and 1-bit amplitude control, supporting a codebook size of 128, *i.e.*, 128 different beam patterns.

Following a similar architecture as in M^3 [82], we disconnect the network interface card (NIC) which is originally connected to the PAMs, and implant a custom-designed radar front-end board in between, as shown in Fig. 3(a). We use an external control FPGA to reproduce the PAM control commands to facilitate real-time control and synchronization. We use a triplexer on the radar front-end board to combine the chirp signal, the control signal (118 MHz), the LO signal (7.56 GHz), and the power supply and feed into the PAM together. Since these signals range from 118 MHz to 17 GHz, we select a wideband 4-way splitter, Minicircuits EP4RKU+ [37], to implement the triplexer. To avoid impedance mismatch, a 50 Ω resistor connects the unused port on the splitter to the ground.

To enable phased-MIMO, the phased array beam scanning must be synchronized with the radar waveform, *i.e.*, the beginning of an FMCW chirp needs to be aligned with the start of a new beam pattern. To this end, we use the BPU–an NI USRP N210–to create a synchronization anchor. When the BPU starts sampling the signal, it sends a trigger signal through its GPIO PIN to the chirp synthesizer and the control FPGA. Upon receiving the trigger signal, the chirp synthesizer starts producing chirps, and the control FPGA sends the PAM the enabling and beam scanning commands. The interval of the beam scanning commands is set using a counter on the FPGA to ensure that it aligns with the duration of the chirps. Our experiments verify this design perfectly aligns the chirp synthesis with beam switching (Sec. 5).

3.2 Transmitting Path Design

We generate the frequency sweeping radar chirps using a frequency synthesizer (ADF4159 [3]) and a VCO (HMC587 [4]). A PLL is designed with ADF4159 and HMC587 to produce a linear, low-phase noise chirp signal, as shown in Fig. 4. ADF4159 can be programmed through a simple 3-wire interface and therefore the chirps with different parameters (such as duration, slope, frequency range, *etc.*) can be synthesized. A graphic user interface provided by Analog Devices is used to configure the chirp synthesizer. Alternatively, the controlling commands can be sent by FPGA for real-time configuration.

As HMC587 can only support a frequency range of 5–10 GHz, we adopt a *2-stage chirp synthesizer design* to meet the desired IF frequency of HybRadar. Specifically, we first generate a 6.5–8.5 GHz chirp signal and subsequently add a frequency doubler (HMC814 [5]) to double the frequency to 13–17 GHz. The original signal is not completely eliminated by the frequency doubler, and the resulting leakage may cause interfering harmonics. We thus add a high-pass filter XHF-143M+ [35] at the following stage to further attenuate the 6.5–8.5 GHz signal.

To perform the Tx-Rx mixing required by an FMCW radar, another copy of the chirp signal is needed. We thus add a power splitter (Minicircuit EP2RKU+ [34]) to split the chirp signal along 2 ways, one to the Tx PAM, and the other to the Rx mixer. Eventually, the Tx PAM upconverts the chirp signal to the mmWave band and emits a 58–62 GHz chirp.

[1]Now discontinued, but can be replaced with Microtik wAP 60Gx3 [33].

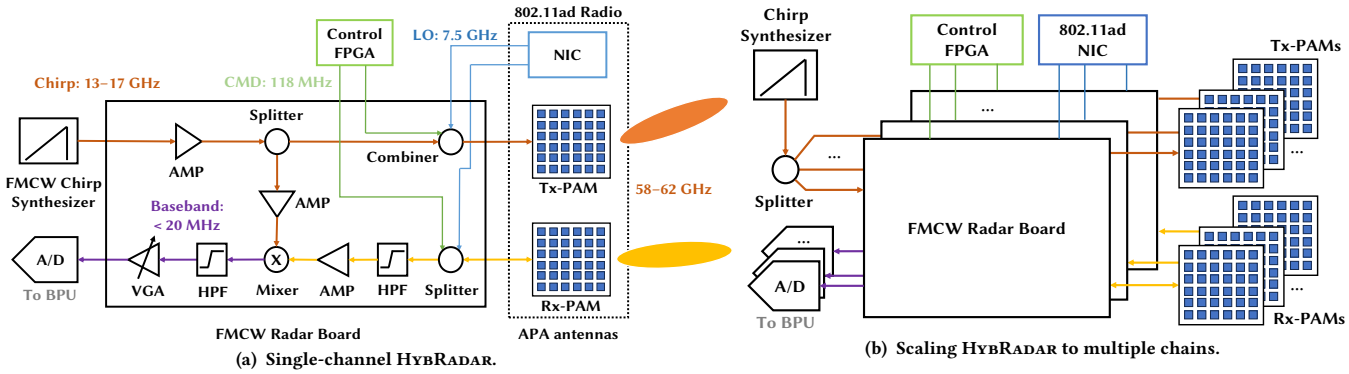

(a) Single-channel HybRadar. (b) Scaling HybRadar to multiple chains.

Figure 3: HybRadar architecture. The architecture is highly modular and scalable.

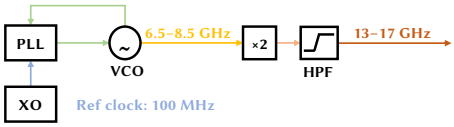

Figure 4: Chirp synthesizer.

3.3 Receiving Path Design

The transmitted FMCW signals are reflected by the objects in the environment and received by the Rx PAM, which subsequently downconverts the signals back to 13–17 GHz. The output signals from the Rx PAM are just a replica of the Tx chirp but with time delays proportional to the range of the reflecting objects. Afterward, the Tx-Rx chirp mixing produces the beat signal that embodies the range information.

The receiving path of the radar front-end board comprises 3 components: the high-pass filter (HPF), the amplifier (AMP), and the mixer. The HPF prevents the 7.56 GHz LO signal from entering the receiving path because otherwise the LO signal, typically stronger than the Rx chirp signal, may saturate the Rx amplifiers. We select XHF-143 [35] as the HPF which features a cutoff frequency of 11 GHz, imposing around 30 dB attenuation on the 7.5 GHz signal with a negligible impact on the 13–17 GHz chirp. In addition, XHF143 is also a reflectionless filter that exhibits a 50 Ω impedance at the stopband, which does not cause any impedance mismatch for the LO and command signal at the triplexer ports, thus ensuring signal integrity.

Although the Rx chirp signal has already been amplified in the Rx PAM, it suffers attenuation from various sources, such as cables, connectors, triplexers, and transmission lines. Therefore, it is essential to amplify the Rx chirp signal before it enters the mixer to maintain a decent SNR. We use Minicircuits AVA-183A+ [36] as the Rx amplifier because it supports a wide bandwidth of 5–18 GHz which covers the desired 13–17 GHz chirp bandwidth. Moreover, AVA-183A+ features a ±1.2 dB gain flatness which ensures a flat frequency response of our wideband chirp signal. We cascade 2 AVA-183A+ to obtain a sufficiently strong Rx chirp signal.

We use HMC8191 [6] as the mixer which supports a wide bandwidth of 6 GHz–26.5 GHz to perform dechirping and produce the baseband beat signal. Notably, HMC8191 is an I/Q mixer that produces two signals, IF1 and IF2, which are 90° out of phase. I/Q mixer structure is often adopted in FMCW radar design because it cancels half of the noise signal and achieves a 3 dB SNR gain [47]. I/Q samples also facilitate the baseband signal processing since the phase of each sample is directly available. In addition, since HMC8191 is a passive mixer and requires a high signal drive power of 18 dBm, we add another AVA183A+ amplifier between the Tx chirp diplexer and the mixer.

3.4 Baseband Circuit Design

After the dechirping process, the beat signal containing essential sensing information is produced. The beat signal bandwidth (~10s MHz) is much narrower than the chirp (4 GHz), which relaxes the ADC sampling rate and simplifies baseband processing.

The baseband circuit achieves two functions: *direct path image filtering* and *baseband signal amplification*. As the radar transmits and receives signals, the Tx signal can propagate to the Rx antennas, causing a direct-path leakage signal. Due to the close proximity between the Tx and Rx antennas, the leakage signal results in a strong close-to-DC image in the baseband signal spectrum. Therefore, an HPF is designed to suppress the low-frequency interference which can improve the linearity of the baseband amplifier.

We determine the cutoff frequency of the HPF by identifying the near-zero peak of the baseband spectrum when no real target is present. The cutoff sharpness of the filter is of top design priority, as the HPF should aim to suppress only the direct path image but not other frequency components corresponding to close-by real radar targets. We, therefore, opt for Chebyshev HPF as it exhibits a sharp cutoff transition region. More specifically, we design a 5th-order Chebyshev filter with discrete LC components.

The strength of the reflected radar signal can vary significantly due to different environments. To fully exploit the dynamic range of the ADC, we employ a variable gain amplifier (VGA) at the baseband. When the signal is strong and ADC clipping is observed, the VGA gain should be tuned down. Otherwise, it should be maximized to detect weak reflecting objects. We use the TI LMH6882 [58] as the baseband VGA to allow for controllable amplification. LMH6882 is a 2-channel programmable gain amplifier with a gain range of 6 dB to 26 dB. The gain can be configured manually using mechanical switches.

3.5 Expanding to Multiple RF Chains

The 1Tx-1Rx module design can easily be expanded to multi-TX-multi-RX by stacking multiple instances of the FMCW radar front-end board, as shown in Fig. 3(b). To achieve coherency between

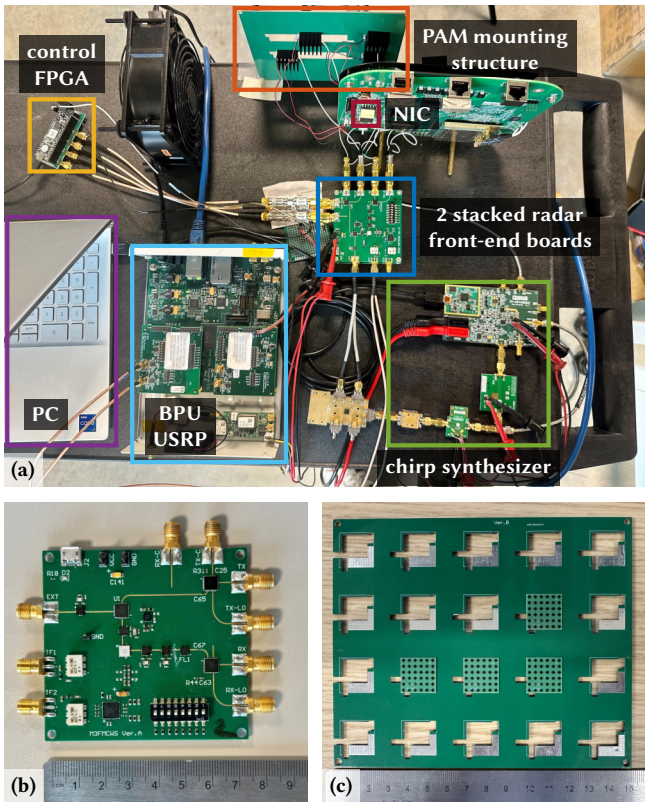

Figure 5: (a) HybRadar with a 2Tx–2Rx setup. The chirp synthesizer and the control FPGA can be further integrated to reduce form factor. (b) Radar front-end PCB. (c) PAM mounting structure.

multiple radar channels, the chirp, LO, and command signals on different channels should be synchronized. We use an RF splitter (EP4RKU+ [37], same as in Sec. 3.1) to create multiple identical copies of the chirp signal and feed them into the stacked FMCW radar front-end boards. Notably, the RF splitter causes *phase unbalance* among the different output ports. For the 13–17 GHz chirp signal, the maximum phase unbalance is 5.3° [37]. Moreover, the cable or PCB traces are not perfectly length-matched which also introduces phase offsets. Nonetheless, these phase offsets are time-invariant, because either the chirps or the LO are synthesized from the same clock source. Therefore, calibration can be performed and phase offsets compensated using standard MIMO radar calibration techniques [8].

Fig. 5(a) portraits an example 2Tx–2Rx HybRadar setup, where two of the radar front-end boards (Fig. 5(b)) are stacked. We have also designed several different PAM mounting structures that allow for customized subarray location (shown in both Fig. 5(c) and 5(a)).

4 PHASED-SUBARRAY LAYOUT AND SIGNAL PROCESSING

Using classical FFT processing [7], the baseband signals of an FMCW radar can be decoupled into multiple *range bins*. Within each range bin, we can obtain a 2D channel matrix $\mathbf{H}$, comprised of the radar backscatter channel from each Tx antenna element to each Rx antenna element. A direction of arrival (DoA) spectrum can be further extracted from $\mathbf{H}$, from which we can estimate the relative angles of targets.

4.1 Radar Channel Estimation

Consider a setup with N_T Tx antennas and N_R Rx antennas and M_T Tx beams combined with M_R Rx beams (totaling $M_T M_R$ scans). The observed radar channel matrix $\mathbf{Y}$ is expressed as:

$$\mathbf{Y} = \mathbf{W}_r^{\mathrm{H}} \mathbf{H} \mathbf{W}_t + \mathbf{N}. \tag{1}$$

Here, $\mathbf{W}_t = [\mathbf{u}_1, \mathbf{u}_2, \ldots, \mathbf{u}_{M_T}]$ and $\mathbf{W}_r = [\mathbf{v}_1, \mathbf{v}_2, \ldots, \mathbf{v}_{M_R}]$ represent the Tx and Rx beamforming weight vectors respectively, where $\mathbf{u}_m \in \mathbb{C}^{N_T \times 1}$ and $\mathbf{v}_m \in \mathbb{C}^{N_R \times 1}$. $\mathbf{N}$ denotes noise. HybRadar's beamformer features a 2-bit phase (0, $\pi/2$, π and $3\pi/2$) and 1-bit amplitude (on/off) (Sec. 3.1). Due to the length difference of the feedline, each antenna has an extra fixed phase offset, which can be obtained through a standard one-time calibration [82]. The effective $\mathbf{W}_r$ and $\mathbf{W}_t$ in real experiments can therefore be calculated accordingly.

For full-MIMO arrays, $\mathbf{W}_t$ and $\mathbf{W}_r$ can be considered as identity matrices, and the radar channel matrix $\mathbf{H}$ is directly obtained from a single radar snapshot.Contrarily, a phased array, due to its inherent analog beamforming component, can only obtain the weighted summation of $\mathbf{H}$. Consequently, a phased array needs to make multiple radar snapshots with varying Tx/Rx beam patterns to recover $\mathbf{H}$.

Exhaustive beam scanning. The baseline method scans at least a full set of $N_T N_R$ beams [81]. For example, firstly, the Tx PAM is fixed to beam #1 while the Rx PAM iterates from beam #1 to #N_R; then similarly, Tx PAM fixes to beam #2, #3 ... #N_T, while the Rx PAM scans all the N_R beams. Orthogonal beam sets, such as discrete Fourier Transform (DFT) based beam sets, are commonly employed to ensure full rankness of Eq. (1). $\mathbf{H}$ can then be effectively estimated by solving Eq. (1) using the Least Squared (LS) method.

Compressive sensing (CS). CS-based channel estimation methods [12, 39] utilize the inherent sparsity of the mmWave channel [57] and require significantly fewer observations than $N_T N_R$ to estimate $\mathbf{H}$. With a judiciously designed codebook (*i.e.* $\mathbf{W}_r$ and $\mathbf{W}_t$) and sparse recovery algorithms, $\mathbf{H}$ can be effectively estimated even when Eq. (1) is underdetermined. A case study in Sec. 6 demonstrates a compressive beam scanning method, reducing the number of observations to 1/8–1/4.

Sensing time and max velocity. During one complete scan, the radar channel needs to be approximately unchanged. Based on the wireless channel coherence time model [48], the target's maximum velocity supported by the radar can be approximated.

$$V_{\max} = 0.423 \frac{\lambda}{N T_c}. \tag{2}$$

Here λ denotes the wavelength, T_c is the chirp duration, and N is the number of snapshots.

The maximum velocity a phased array radar supports grows inversely with the number of beam scans. A phased-MIMO system comprises multiple independent phased subarrays and requires fewer snapshots than a phased-array system, striking a tradeoff between system complexity and sensing time.

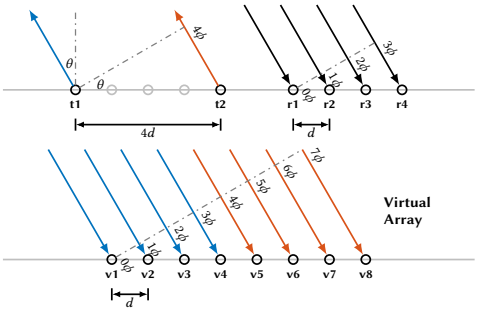

Figure 6: Illustration of the SCA. (v1-v4) = t1 + (r1-r4), and (v5-v8) = t2 + (r1-r4). The summation of the location mirrors the cumulative phase of the wavefront.

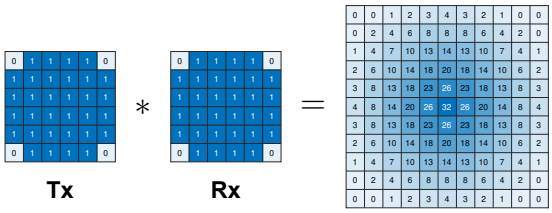

Figure 7: The SCA from 1Tx-1Rx PAM constructed using spatial convolution. The number indicates the overlapping virtual elements.

4.2 Optimizing Subarray Layout

Optimal antenna placement in full-MIMO radar systems is a well-explored area. However, the phased-MIMO architecture introduces additional constraints on antenna locations, necessitating further investigation. This section delves into the optimal arrangement of phased subarrays to create virtual arrays with an expansive antenna aperture, thereby achieving enhanced spatial resolution.

4.2.1 Sum Co-array (SCA) Design. The SCA [25] is a type of virtual array widely employed in active radar sensing where the Tx and Rx elements are coherent and co-located. SCA construction involves determining the spatial *summation* of Tx-Rx element pairs within a physical sensor array. This process effectively transforms the physical array into a configuration comprising a singular Tx element alongside a virtualized Rx array. This transformation is predicated on the principle that the summation of spatial locations mirrors the cumulative phase of the wavefront, a relationship depicted in Fig. 6.

An SCA can be constructed by performing spatial convolution of the Tx array and Rx array [49]. In the case of both the Tx array and Rx array being a $N \times N$ UPA, an SCA of $(2N-1) \times (2N-1)$ can be constructed. The Tx/Rx array in HybRadar is a 6×6 UPA with antennas on the 4 corners disabled. Thus, the corresponding SCA is an 11×11 UPA with 3 elements missing on each corner, as illustrated in Fig. 7. Notably, due to the close spacing of the antennas within the same phased array, a large portion of Tx-Rx pairs synthesize a virtual antenna at the same location, resulting in redundant channel information.

With multiple Tx and Rx phased-arrays, an even larger SCA can be synthesized. To maximize the SCA, the location of the PAMs should be designed to minimize overlapping elements in the virtual array. Since each Tx-Rx phased-array pair synthesizes a $(2N-1) \times (2N-1)$ virtual UPA, if L Tx and K Rx PAMs are placed on a horizontal line to achieve angular resolution on the azimuth plane, the spacing between the phased arrays should satisfy:

$$d_{Rx} = (2N-1)d, \quad d_{Tx} = K\, d_{Rx}, \tag{3}$$

or alternatively, $d_{Tx} = (2N-1)d$ and $d_{Rx} = L\, d_{Tx}$. Consequently, the size of the virtual SCA:

$$N_v = (2N-1)KL. \tag{4}$$

The effective aperture can thus be scaled by multi-folds in comparison to an unspaced placement of the phased arrays. An example is shown in Fig. 8.

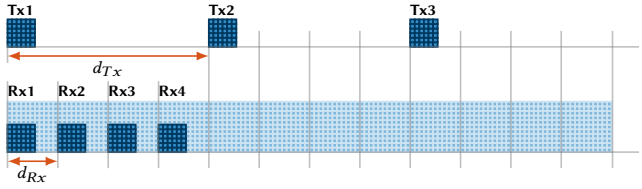

Figure 8: The SCA synthesized by $K = 3$ Tx PAMs and $L = 4$ Rx PAMs with UPA dimension $N = 6$. The light blue squares represent the resulting virtual array (11×132).

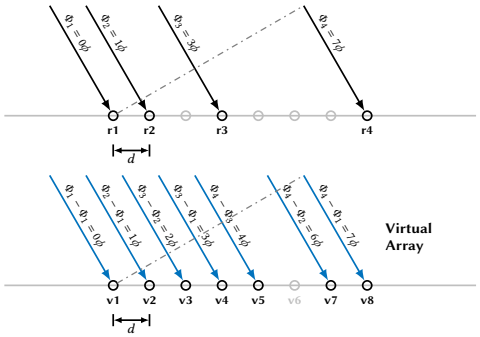

Figure 9: Illustration of the DCA. The differences of the locations mirror the phase differences of the wavefront. Element v6 is missing since 5ϕ can not be found in the phase differences.

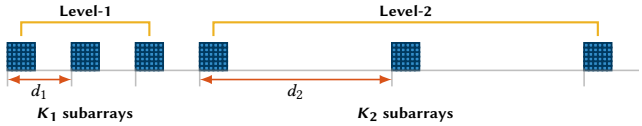

Figure 10: 2-level NAS. The subarrays in the same level follow a uniform spacing.

4.2.2 Difference Co-array (DCA) Design. The DCA is primarily employed in passive sensing scenarios, such as radio astronomy or passive radar systems, where an array of co-located sensors receive signals from uncontrolled, unknown sources. The DCA operates independently from the SCA and can further expand the virtual array's dimensions beyond what the SCA offers. The construction of a DCA involves calculating the spatial location differences between element pairs within an Rx physical array. The construction is based on the principle that the difference of the spatial locations mirrors the difference of the phases of the wavefront at the sensors, which can be found by determining the signal vector's autocorrelation [44].

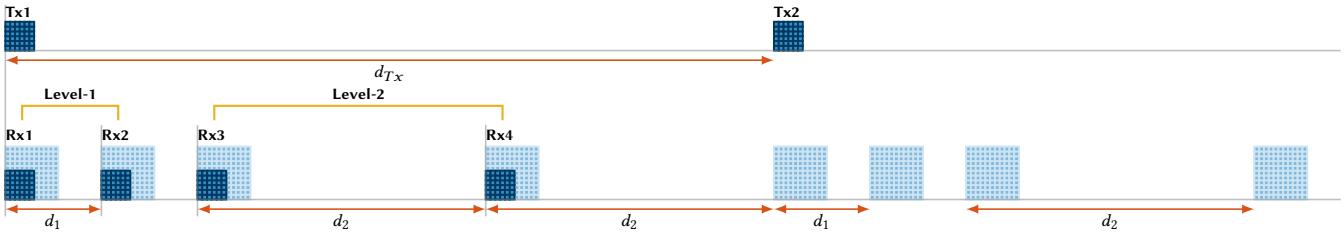

Figure 11: DCSC with nested subarrays. The light blue squares represent the virtual antennas from the SCA. Rx subarrays keep the same geometry as the DCA shown in Fig. 10. Tx2 makes a second copy of the virtual array on the right side.

In classical DCA theory, the signal sources must be assumed to be uncorrelated. In the context of active radar sensing, the "sources" correspond to the reflections from the radar targets, which are originally from the same Tx source. The assumption holds only when the multiple targets experience random yet uncorrelated small displacement over time (*e.g.*, random vibration caused by wind). Since HybRadar operates at 60 GHz mmWave band, the maximum displacement only needs to be around 2.5 mm to cause a phase shift of 2π and randomize the complex radar channel. Notably even if the assumption does not hold, DCA can still be effectively utitlized through techniques like spatial smoothing [10].

To employ DCA in HybRadar, we propose a subarray placement strategy to maximize the aperture of the DCA. This is challenging because given the number of antennas on a straight line, the optimal locations and corresponding DCA size cannot be computed in any closed-form [31]. Consequently, many suboptimal but trackable array geometries have been proposed for DCA synthesis [42, 43, 66]. However, these methods only deal with the element placement in traditional antenna arrays, whereas HybRadar comprises subarrays that constrain the locations of their antenna elements.

We extend the idea of nested array [42], and propose a 2-level nested array of subarrays (NAS) for HybRadar, as shown in Fig. 10. The proposed NAS comprises a level-1 array of K_1 subarrays with spacing d_1 and a level-2 array of K_2 subarrays with spacing d_2, where

$$d_1 = (2N-1)d, \quad d_2 = (K_1+1)(2N-1)d. \tag{5}$$

Notably, the spacing between the first level-2 subarray and the last level-1 subarray is also d_1. In the level-1 subarray, the spacing $(2N-1)$ ensures that the "holes" between the k-th and $(k-1)$-th subarrays can be filled by finding the difference set between the k-th subarray with the 1st subarray. In the level-2 subarray, the spacing is related to the number of level-1 subarrays K_1, and the "holes" between the k-th and $(k-1)$-th subarrays can be filled by finding the difference set between the k-th subarray with all the level-1 subarrays. The total number of virtual antennas

$$N_v = (2N-1)(K_1K_2+K_2-1)+N. \tag{6}$$

Therefore, given the total number of phased arrays K, the goal is to maximize N_v under the constraint that $K_1+K_2=K$. For example, with $K=4$ Rx phased arrays and $N=6$ element on one dimension of the phased array, it can be found through an exhaustive search over a few combinations that when $K_1=2, K_2=2$, the dimension of the virtual array is maximized, *i.e.*, $N_v=61$.

4.2.3 Difference Co-array of Sum Co-array (DCSC) Design. The SCA and the DCA can be combined to synthesize a DCSC with even a large aperture [9]. Based on the analysis in Sec. 4.2.1, 1 Tx and 1 Rx phased array can be equivalently seen as one single Tx antenna and a $(2N-1)\times(2N-1)$ Rx phased array. Similarly, when there are 2 Tx phased arrays, 2 copies of $(2N-1)\times(2N-1)$ are synthesized. Following the principle, we employ the idea of SCA to create multiple copies of the NAS. Specifically, the Rx phased arrays follow the same 2-level nested array geometry as in Eq. (5) but with $N'=2N-1$. Since each Tx phased array adds another copy of the NAS in Fig. 9, a new Tx PAM should be placed in a location such that the first subarray of the new NAS has the same level-2 spacing with the last subarray of the previous NAS, as shown in Fig. 11. Therefore, the Tx PAMs should follow a uniform spacing given by:

$$d_{Tx} = (2N'-1)(K_1K_2+K_2-1). \tag{7}$$

Thus, the size of the final virtual array scales up to:

$$\begin{aligned} N_v = {} & (2N'-1)(K_1K_2+K_1+K_2)L \\ & -(K_1+1)(2N'-1)+N'. \end{aligned} \tag{8}$$

5 HARDWARE PERFORMANCE EVALUATION

In this section, we conduct microbenchmarks to verify HybRadar's hardware design and virtual array synthesis methods.

Time synchronization across subsystems. As mentioned in Sec. 3.1, the BPU, chirp synthesizer, control FPGA and the PAMs need to be fully synchronized. To verify this, we use an oscilloscope to measure the triggering signal from the BPU, the chirp complete signal from the ADF4159 evaluation board, and the PAM controlling signal from the FPGA. As typical chirp durations for commercial automotive FMCW radars are in the order of 10s of µs [59], we set the chirp duration to be 90 µs with a 10 µs inter-chirp idle period. The chirp idle period is inserted to mitigate the noise introduced when the chirp is reset to the starting sweep frequency [59]. Fig. 12 shows that once triggered, the FPGA sends commands right at the time when one chirp synthesis is complete, and this happens with a period of 100 µs as expected. The PAM responds to the commands after a delay of 170 ns, and the exact start-up timing can be found in [82]. In the current prototype, the clock of the FPGA is not synchronized with the rest of the system, causing a slight time offset for each chirp. Through measurement, we find the accumulated time offset after sending 10k chirps is 1.5 µs. However, the beam switching command does not need to be perfectly synchronized; it only needs to be issued during the inter-chirp idle time (10 µs) so that the beam pattern is aligned with each chirp. For long-time continuous radar sensing applications, the BPU can always send repeated triggering signals to regain synchronization. The experiment verifies *HybRadar's subsystems are synchronized and that each beam scan is aligned with each FMCW chirp.*

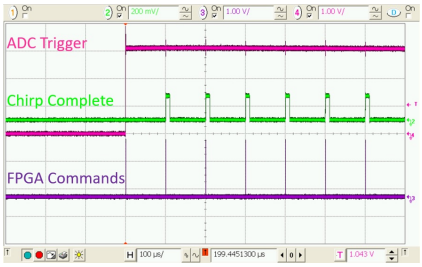

Figure 12: Subsystem synchronization.

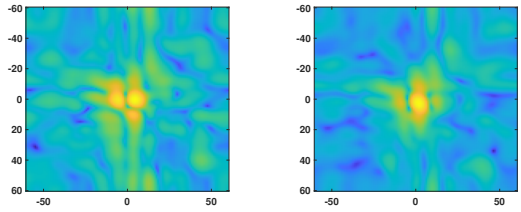

(a) Before calibration. **(b) After calibration.**

Figure 13: 2D Angular spectrum synthesized using the multi-channel radar.

Multi-channel calibration. HybRadar requires a one-time calibration to compensate for the phase/amplitude variations across different Tx-Rx pairs. We follow a common MIMO radar calibration procedure to perform calibration for a representative 2Tx–2Rx HybRadar setup. We put a trihedral corner reflector at a distance of 7.5 m at the boresight as a reference target, and enable each Tx-Rx PAM pair to sense the target with a fixed beam. We perform range FFTs (with zero-padding to improve accuracy) and identify the range bins with the highest amplitude. We then compare the phase/amplitude differences and compute the complex calibration vector.

To show the effectiveness of the calibration, we move the corner reflector to a different location and perform range and angular analysis. If the calibration factors are not applied, the angular spectrum exhibits multiple strong lobes (Fig. 13(a)) due to the phase offset among the Tx-Rx pairs. Once compensated, the split lobes are eliminated (Fig. 13(b)), which verifies the *effectiveness of the calibration across RF chains and PAMs.*

Angular resolution with multiple Tx-Rx PAMs. To evaluate the effectiveness of sparse array synthesis for HybRadar, we conduct experiments measuring angular resolution across different co-array setups. We place 2 identical trihedral corner reflectors in front of the radar at around 7.5 m and gradually reduce the separation between the targets until they become undistinguishable in the angular spectrum. The theoretical angular resolution for beamforming-based DoA estimation is described by $\theta_{res} \approx 0.89\frac{\lambda}{Nd\cos\theta}$ [56]. Here the antenna spacing $d = 0.58\lambda$, N is the number of antennas, and θ is the target angle relative to the antenna array. Without loss of generality, we only measure the horizontal angular resolution.

In our first experiment, we employ the SCA configuration with varying numbers of Tx/Rx PAMs, *i.e.* 1Tx–1Rx, 1Tx–2Rx, 1Tx–3Rx, and 2Tx–2Rx. The spacing between the Rx PAMs d_{Rx} is designed to be $11d$, aligning with Eq. (3). Also from Eq. (3), $d_{Tx} = 22d$ for

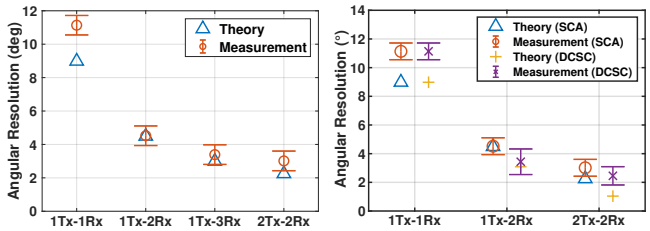

(a) SCA with increased PAM count. **(b) SCA vs. DCSC.**

Figure 14: Angular resolution measurement result.

the 2Tx–2Rx setup. With such a configuration, the size of the virtual array is $N_v = (11, 22, 33, 44)$ following Eq. (4). As a prototype HybRadar, we only fabricated 2 Rx chains. So we emulate the 3rd Rx-chain by repositioning a PAM and combining the data from 2 measurements. Fig. 14(a) shows that the angular resolution improves as the number of PAMs increases, although it falls short of the theoretical value due to practical limitations such as PAM spacing tolerance, corner reflector size, and SNR.

In our second experiment, we measure the angular resolution with the DCSC setup in Fig. 11 with varying numbers of PAMs, including 1Tx–1Rx, 1Tx–2Rx, and 2Tx–2Rx. Based on Sec. 4.2.3, for 1Tx-1Rx, the virtual array is the same as an SCA. For 1Tx-2Rx, the DCSC reduces to $K_1 = 1, K_2 = 1, L = 1$. For 2Tx–2Rx, $K_1 = 1, K_2 = 1, L = 2$. According to Eq. (8), the horizontal dimension of the virtual array is $(11, 32, 95)$, respectively, which corresponds to a theoretical value of $8.98°$, $3.09°$, and $1.04°$. The result in Fig. 14(b) affirms that the DCSC configuration offers an improvement in angular resolution with the same number of Tx/Rx chains. Notably, there remains a gap between the measured resolution to the theoretical resolution. Apart from the measurement error mentioned above, the gap also stems from the unsatisfied assumption of uncorrelated sources (Sec. 4.2.2) in practical experiments.

Table 2 compares HybRadar with 2Tx–2Rx setup with the state-of-the-art (SOTA) mmWave radar systems. The angular resolution is measured using a similar setup described above employing SCA only. For the 1D horizontal-only case, with only 4 RF chains, HybRadar achieves a better angular resolution than VTRIG-74. TI mmWCAS achieves a superior resolution, but it cannot achieve 2D resolution simultaneously due to its antenna layout. In the 2D case, HybRadar achieves a comparable angular resolution with VTRIG-74 with only 1/10 of the RF chain count which implies a much lower system complexity, cost, and power budget. However, with a similar number of virtual elements, HybRadar requires 10–20 times more snapshots than VTRIG-74, which increases the sensing time and compromises its sensing ability for moving targets (Eq. (2)).

Radar link budget analysis. The capability of a radar to detect a target is fundamentally linked to the SNR of the received signals, which follows the well-known radar equation [56]:

$$\text{SNR} = \frac{\sigma P_t G_{ant}^2 G_{tx} G_{rx} \lambda^2}{(4\pi)^3 d^4 k T B_n F}. \tag{9}$$

Here, σ represents the radar cross section (RCS) of the target. Extracted from the datasheet from Airfide [1], the single-chain transmission power $P_t = 6$ dBm, and the gain of each antenna element $G_{ant} = 5$ dBi. G_{tx} and G_{rx} denote the respective Tx/Rx array gains, which grow proportionally with the number of active antennas.

Table 2: Performance comparison with SOTA radars.

System	RF Chains	Architecture	Ang. Res. (°)	Virtual Elem.	Min. Scans[2]	Scan. Time[3](µs)	Max. Velocity (m/s)
MMWCAS-RF-EVM [60]	9T–16R	full-MIMO	**H**: 1.5,[1] **V**: N/A	86	9	450	4.70
VTRIG-74-1D [67]	1T–20R	full-MIMO	**H**: 7.6, **V**: N/A	20	1	50	42.3
HybRadar-1D	2T–2R	phased-MIMO	**H**: 3.0, **V**: N/A	44	22	1,100	1.92
VTRIG-74-2D [67]	20T–20R	full-MIMO	**H**: 7.6, **V**: 7.6	400	20	1,000	2.11
HybRadar-2D	2T–2R	phased-MIMO	**H**: 3.0, **V**: 11.1	436	218	10,900	0.194

[1] From published data [62]. [2] Ideal case without any redundant scans that result in overlapping virtual elements. [3] Chirp duration = 50 µs.

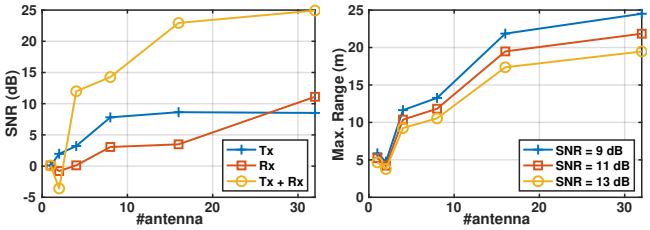

(a) Signal-to-noise ratio. (b) Detection range.

Figure 15: The array gain with the increasing number of Tx/Rx antennas.

Other factors include the carrier wavelength $\lambda = 5$ mm, the target's distance d, the Boltzmann constant $k = 1.38 \times 10^{-23}$ J/K, and T, the temperature measured in Kelvin. The noise bandwidth in FMCW radar $B_n = 1/T_c$ where $T_c = 90$ µs is the chirp duration in our experiments. The receiver's noise factor $F = 8.5$ dB is determined by the PAM's RF character.

We define the *maximum detection range* as the distance when the SNR falls below a pre-specified threshold, which in turn depends on the desired detection accuracy [56]. For example, the required SNR to detect a target with a probability of 0.9 and a false detection rate of 10^{-3} is 11 dB [56]. To characterize the G_{tx} and G_{rx}, we place a corner reflector at the boresight of the radar and sense the target with an incrementally growing count of active antennas. The phase shifters in the beamformers are configured to Tx/Rx boresight beams. Fig. 15(a) shows an SNR augmentation of approximately 25 dB, when all the Tx and Rx antennas are active, relative to a singular Tx and Rx antenna configuration. Correspondingly, Fig. 15(b) exhibits the maximum detection range receiving a boost of around 20 to 25 meters as the antenna count increases. The result substantiates *the effectiveness of the antenna array in elevating target detectability.*

We further measure the SNR of common radar targets at a fixed range with multiple Rx PAMs and then follow Eq. (9) to estimate the link budget. The Rx PAMs are placed on a 2×2 array with all the antennas enabled. As a prototype with only 2 Rx chains, the 2×2 array is a virtual array emulated using 2 Tx PAMs through time division following the SCA principle (Sec. 4.2.1).

Table 3 shows that even with the 1Tx-1Rx setup, most common objects can be detected at a range > 12 m. Human does not reflect radar waves as strongly as other objects but the detection range is sufficient for short-range indoor applications. The maximum detection range can further increase with more Rx channels. The impact of multiple Tx PAMs is similar, and therefore not further evaluated. Notably, due to practical factors such as calibration residual and radar channel diversity across the PAMs, the SNR gain from coherent combining does not simply increase linearly. This demonstrates the capability of HybRadar as a research platform for *short to mid range phased-MIMO radar experiments.*

We note that, theoretically, the phased array beam patterns manifest only in the radar's far-field. For example, for a 1 Tx and 4 adjacent Rx arrays, this is around 5.5 m following the far field model [40], still well within the detection range of HybRadar. For even larger array of subarray geometries, the far-field may exceed the detection range. However, note that the far-field model is only an approximation. Even within the near-field, the beam patterns' mainlobes still dominate, albeit distorted and hence reducing the effective array aperture from the theoretical maximum.

Table 3: Detection range of common objects.

Object	SNR@10 m 1T–1R (dB)	Max. Range 1T–1R (m)	Max. Range 1T–2R (m)	Max. Range 1T–4R (m)
Corner Reflector (12 dBm^2)	24.58	21.85	24.83	23.82
Human	5.48	7.28	8.76	11.87
Bicycle (Side)	19.25	16.08	22.82	24.82
Sedan (Front)	24.92	22.28	31.47	33.76
Post (Square)	26.09	23.84	26.49	31.64
Tree	12.22	10.73	13.63	15.39
Trash Bin	15.22	12.75	17.22	16.34

System cost. The cost breakdown of HybRadar is detailed in Table 4, which reveals that the cost of the RF front-end of the digital and analog radar are similar. However, the need for wideband baseband processing in digital radars leads to a noticeable increase in overall system cost. Despite its prototype status, HybRadar's cost is comparable to start-of-the-art radar systems, as indicated in Table 5. Replacing the USRP N210 with a low-end FPGA and a low sampling-rate multi-channel ADC (20 MHz is sufficient) could substantially reduce the cost. Moreover, integrating the FMCW front-end board and the chirp synthesizer into ICs can further improve cost efficiency.

Table 4: System cost breakdown.

Component	Unit Price	2Tx–2Rx Analog	2Tx–2Rx Digital
FMCW Front-end Board	$786	2	0
Chirp Synthesizer	$667	1	0
M^3 Bridge Board[82]	$938	0	2
RFSoC Adapter Board	$437	0	1
Airfide Radio	$700	1	1
Front-end Total		$2,939	$3,013
USRP N210	$3,354	1	0
Xilinx RFSoC	$11,658	0	1
System Total		$6,293	$14,671

Table 5: Cost comparison with SOTA mmWave radars.

Reference	Fc (GHz)	BW (GHz)	Tx/Rx Ch.	Ant.	Cost† (USD)
AWR1642BOOST [61]	76–81	4	2/4	6	$299
MMWCAS-RF-EVM [60]	76–81	4	12/16	28	$1,462
TEF82-R294-KIT [41]	76–81	4	6/8	14	$3,400
VTRIG-74 [67]	62–69	7	20/20	40	$3,444
Han *et al.* [19]	60.8	0.4	2/2	64	N/A
HybRadar-1	58–64	4	2/2	**128**	$2,939
HybRadar-2	58–64	4	4/4	**256**	$4,510

† The cost only comprises the RF front-end.

6 CASE STUDIES

6.1 3D Point Cloud Generation

In this section, we showcase the capability of HybRadar in synthesizing high-resolution 3D radar point cloud images.

Hardware setup. Illustrated in Fig. 17(a), our setup incorporates 2 Tx PAMs aligned vertically and 2 Rx PAMs in a horizontal layout, both maintaining a central gap of $11d$. We employ the SCA array synthesis (Sec. 4.2.1) which is suitable for stationary targets (Sec. 4.2.2). With a 1Tx-1Rx combination, we obtain an 11×11 virtual array, equating to an angular resolution of 8.98° across both axes. In contrast, the 2Tx–2Rx amalgamation yields a 22×22 virtual array, refining the angular resolution to 4.49°. This configuration is appropriate when imaging precision is of equal importance in both dimensions. The 2 Tx PAMs operate in a time division manner while the Rx PAMs remain constantly active.

The chirp bandwidth is maximized to 4 GHz to achieve a fine-grained range resolution of 3.75 cm. Following a similar configuration to commercial FMCW radar [59], the chirp duration and the inter-chirp idle duration are respectively set to 90 µs and 10 µs.

Phased-MIMO radar 3D point cloud workflow. Our procedure for 3D radar imaging using HybRadar is depicted in Fig. 16. We follow the exhaustive beam-scanning approach detailed in Sec. 4.1. Considering each PAM as a 6×6 UPA, the steering matrix is generated using the Kronecker product of two 6×6 DFT matrices [70, 76], resulting in a dimension of 36×36. Factoring in the 4 inactive corner antennas, the actual dimensions reduce to 36×32. After scanning 36×36 chirps, the observation matrix $\mathbf{Y}$ (Eq. (1)) is acquired after performing the range FFTs. For each relevant range bin, the channel matrix $\mathbf{H}$ can be subsequently obtained by performing LS estimation. Next, employing the SCA principle, a 22×22 virtual array is derived. The missing elements in the virtual array caused by the 4 inactive corner antennas are filled with zeros.

Subsequently, the MUSIC algorithm [51] is employed on the virtual array to discern the DoA of reflective points. The steering vector used in MUSIC aligns with the angle definition in Fig. 17(b). In active radar sensing, since target-reflected signals are coherent, we employ spatial smoothing [54, 69] for enhanced MUSIC output. For the 1Tx–1Rx PAM setting, we use the redundancy in the phased array radar channel and perform joint transmitter smoothing as in [79]. For the 2Tx–2Rx arrangement, with missing central elements due to the inactive corner antennas, spatial smoothing is executed over the 4 individual 11×11 virtual arrays, each corresponding to a Tx-Rx pair. Upon obtaining the MUSIC pseudo-spectrum, a pre-defined threshold filters out valid (range-angle) data points, culminating in the final 3D point cloud.

Experimental results for 3D point cloud generation. We choose a human subject to showcase the imaging performance, under 3 hardware setups: (a) 1 single Tx antenna + 1 Rx PAM; (b) 1 Tx PAM + 1 Rx PAM; and (c) 2 Tx PAMs + 2 Rx PAMs. The corresponding virtual array sizes are 6×6, 11×11, and 22×22, respectively. Fig. 18 shows the front and top view of the subjects with different postures. Setup (a) possesses the smallest virtual array size and does not have any redundant channels, resulting in a poor SNR, sparse point cloud, and lots of ghost points. Employing 2 PAMs in setup (b), the contour of the subjects becomes distinguishable and ghost points are mitigated. Setup (c) quadruple the number of observations compared with (b). With the spatial diversity offered by the extra Tx-Rx channels, more details of the subject can be distinguished, and the point cloud shape highly resembles the ground truth. Multiple Tx-Rx PAMs allow for more degrees of freedom for spatial smoothing, effectively suppressing the noise and ghost points.

The result highlights the phased-MIMO radar's capability to generate high-resolution point clouds. The employed exhaustive scanning method necessitates the scanning of 2,592 beams (36×36×2) for each scanning session. Due to the long scanning time, the method is best suited for scenarios where the targets exhibit minimal movement such as detailed environmental mapping.

6.2 Compressive Radar Beam Sensing

As discussed in Sec. 4.1, a phased-MIMO radar with large phased-subarrays requires a significantly longer sensing time than a full-MIMO radar, which makes real-time sensing cumbersome. CS [12], which has already found applicability in fast beam alignment for mmWave communication devices [11, 16, 27, 28, 39, 71], emerges as a potential solution for efficient radar sensing as well. In this case study, we demonstrate a quick scanning method for phased-MIMO radar using CS.

Problem formulation. CS radar channel estimation utilizes the mmWave channel sparsity to reduce the number of beams. The sparsity indicates that there only exists a few directions where the Tx signal is reflected into Rx. Mathematically, it means the beamspace matrix $\mathbf{X}$, defined as the 2D-DFT of $\mathbf{H}$, has only a few non-zero elements. Eq. (1) can be reformulated into the standard CS framework [12, 29] as

$$\mathbf{y} = \mathbf{Q}\mathbf{x} + \mathbf{v}. \tag{10}$$

Here $\mathbf{y} \in \mathbb{C}^{m\times 1}$ represents the vectorized observation matrix $\mathbf{Y}$; $\mathbf{Q} \in \mathbb{C}^{m\times n}$ is the sensing matrix derived from $\mathbf{W}_t$ and $\mathbf{W}_r$; $\mathbf{x} \in \mathbb{C}^{n\times 1}$ stands for the sparse beamspace vector transformed from the original channel matrix $\mathbf{H}$ and $\mathbf{v} \in \mathbb{C}^{m\times 1}$ denotes the noise vector.

With limited beam scans, Eq. (10) is underdetermined ($m < n$). Sparse recovery techniques like orthogonal matching pursuit (OMP) [65] and sparse Bayesian learning (SBL) [64] are commonly used to solve for $\mathbf{x}$ utilizing its sparsity. The estimated beamspace vector $\mathbf{x}$ can then be transformed back to the original channel matrix $\mathbf{H}$.

Codebook design for compressive beam scanning. Considering the unique phased-MIMO architecture of HybRadar, we propose a custom CS codebook design. The design of the codebook for CS aims to minimize the total coherence of the sensing matrix $\mathbf{Q}$ [13], a measure of correlation among beam patterns. Considering the optimal codebook form provided in [29, 78] and HybRadar's

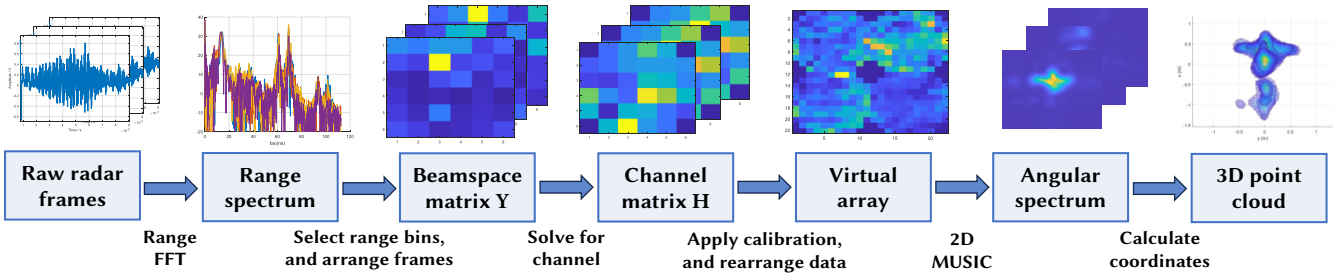

Figure 16: Radar 3D point workflow.

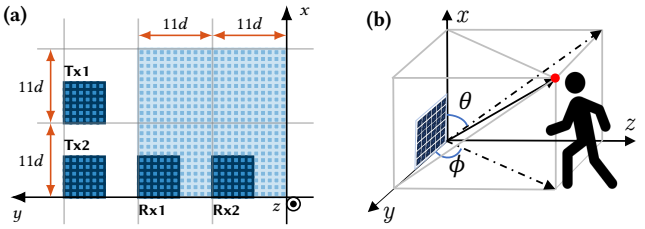

Figure 17: (a) PAM placement and corresponding virtual array. (b) Coordinate system.

hardware constraint (32 elements/PAM with 2-bit phase shifters), we base our design on Hadamard matrices [23]. Hadamard matrices based codebook possesses two essential attributes: *(i)* Elements being either ±1, favoring the low-resolution phase shifters; *(ii)* Recursive construction, facilitating scalability with a large number of PAMs. The construction results in a full codebook with a size equal to the number of Tx-Rx antenna pairs. We subsequently select a subset of the complete codebook for compressed radar beam scanning. To enhance robustness, the selection of beams follows two empirical principles: full spatial coverage and inter-beam overlap. Additionally, other beam sets like the DFT matrix-based codebook [76] and the random codebook are generated to serve as benchmarks. Typical beam shapes are displayed in Fig. 19.

Experimental results for compressed radar beam scanning. To validate the efficiency and efficacy of the proposed CS-based radar beam scanning, we implement and use it to detect a target (corner reflector) randomly placed at 40 positions (between 1.7 m and 7.1 m from the radar). Fig. 20(a) presents the angular accuracy and error rate with an increased number of Rx PAMs. An angular estimation error is declared when the estimated angle deviates from the ground truth by over 10°. We compare different CS methods against a baseline LS method, which requires transmission across all possible 32×32 beam pairs. As expected, with the same beam scanning time, the angular accuracy improves with the number of Rx PAMs. Notably, the simpler, greedy algorithm, OMP, does not match up to the more intricate ℓ_1-minimization-based SBL approach [72], underscoring the trade-off between computational simplicity and performance.

Fig. 20(b) contrasts the angular accuracy against the count of scanned beam pairs. Our designed codebook achieves commendable performance with just a quarter of the beam pairs in full-MIMO. Contrarily, the randomly selected DFT codebook exhibits subpar performance. Its primary setback is the narrow concentration of each beam, causing the chosen beams to inadequately span the entire space with minimal overlap. The random codebook, on the other hand, exhibits an overly broad beam pattern, that leads to a reduced SNR, thus lagging behind our designed codebook in performance.

The CS algorithm can be further optimized by incorperating two factors. (1) The co-located Tx/Rx antennas result in identical AoA and AoD in radar sensing, which provides additional prior knowledge. (2) The current virtual array design introduces redundancy (Sec. 4.2.1) that could be optimized to reduce the number of beam scans. Addressing these issues could drastically boost sensing speed, enabling phased-MIMO radars to operate in highly-dynamic environments such as autonomous driving and drone navigation.

7 DISCUSSION

Scaling towards a massive phased-MIMO radar. Our present hardware configuration supports a maximum of 4Tx and 4Rx channels, restricted by the NIC's 8 LO ports (Sec. 3.1). A potential route to system expansion involves substituting the NIC with an external clock synthesizer (*e.g.* TI LMX2595[63]). To supply LO to more than 8 channels, a clock distribution network comprising splitters and amplifiers needs to be designed, ensuring phase coherence and sufficient power delivery. The FPGA embedded within the system can handle all the PAM command signals, and custom sources can provide DC power supply.

The limited benefit of Tx phased array. In practical applications, since the Tx power is regulated by maximum effective isotropic radiated power (EIRP), which necessitates power adjustments during beamforming, the Tx phased array provides no SNR gain. In addition, due to the close antenna spacing, employing phased arrays on both Tx and Rx results in numerous overlapping elements in the virtual array. It provides limited improvement of angular resolution while greatly increasing the sensing time (Sec. 4.1). Therefore, a better design tradeoff might be employing phased-MIMO on the Rx side while maintaining full-MIMO on the Tx side. HybRadar can realize this setup by enabling only one antenna on the Tx phased array.

8 RELATED WORK

COTS mmWave radars. TI's AWR1642BOOST [61] is a widely used automotive radar sensor module with 2Tx–4Rx RF chains. Its limited antenna count, however, curtails its angular resolution. In contrast, TI MMWCAS-RF-EVM [60] boasts a total of 12Tx–16Rx RF chains. These antennas, mainly aligned horizontally, prioritize high angular resolution in the azimuth plane, ideal for automotive contexts. Another notable device, NXP's TEF82-R294-KIT [41], integrates 6 Tx–8 Rx RF chains, again oriented horizontally. Vayyar's VTRIG-74 [67] comes equipped with 20Tx–20Rx RF chains.

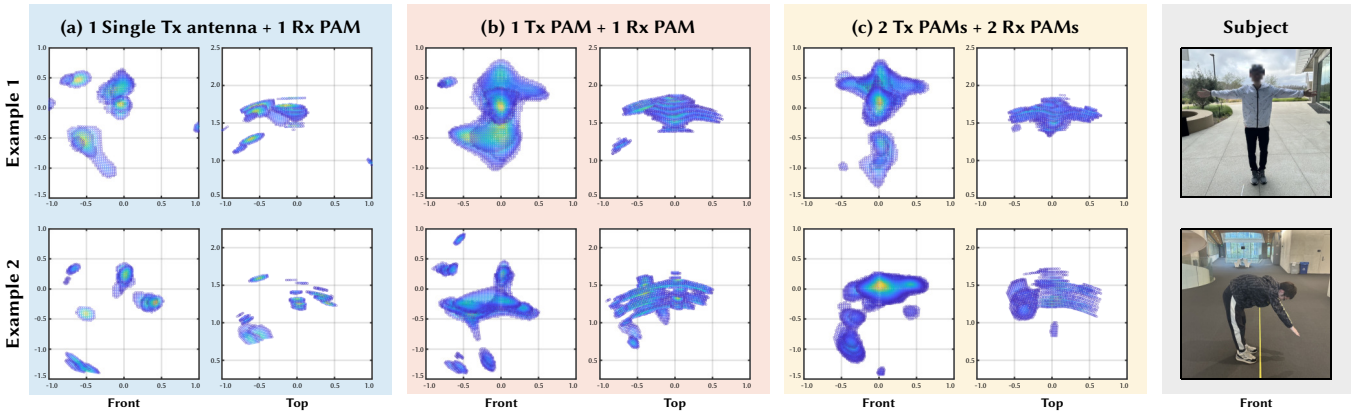

Figure 18: 3D point cloud examples (axis unit: meter).

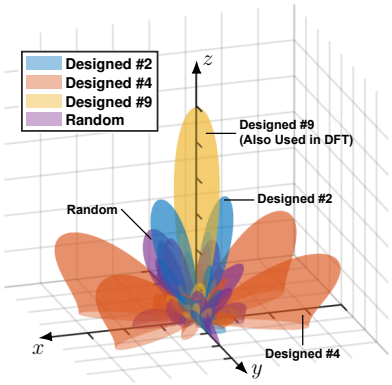

Figure 19: Tx/Rx beam shape examples. DFT beams are highly directional while the random-generated beams exhibit broad beam shapes. The designed CS beams strike a balance.

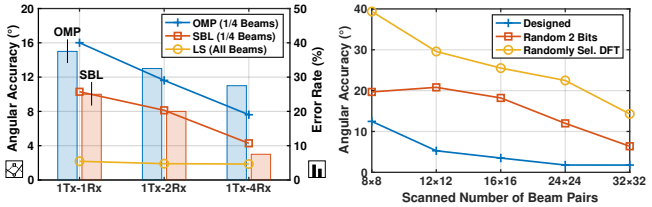

(a) Different CS algorithms. **(b) Different codebooks (1Tx–4Rx).**

Figure 20: Angular accuracy measurement results for compressive sensing based methods. *Error rate of LS is 0, therefore not shown.

Its unique design, with the Tx array perpendicular to the Rx array, facilitates a 20×20 virtual array, ensuring consistent spatial resolution in both directions.

The current platforms predominately adopt a full-MIMO architecture, which lacks scalability under the cost, size, and power constraints. In contrast, the phased-MIMO design is an alternative to overcome these limitations. As a phased-MIMO platform, HybRadar also offers unprecedented flexibility to support novel research in sparse array signal processing, radar imaging, efficient radar beam scanning, *etc.*

mmWave software radio testbed. The advancement of mmWave software radio testbeds has accelerated in recent years, spurred by the increasing demand for experimental platforms for mmWave communication and sensing. OpenMili [80] represents the first 60 GHz SDR equipped with a programmable 4-element phased array, supporting a mere 5 beams. X60 [50] marks another step in the evolution of mmWave SDR platforms, employing a 12-element antenna phased array with real-time configurable Tx and Rx beams. Pi-Radio v1 [83] proposes a mmWave SDR platform with a 4-channel fully digital architecture. M^3 [82] stands out with its fully reconfigurable array of phased arrays, accommodating up to 8 RF chains and impressive 256 antenna elements. Different from M^3, HybRadar is an analog FMCW phased-MIMO radar platform that aims to facilitate radar signal acquisition and processing.

Sparse arrays. The SCA, DCA and DCSC [25, 44] have been studied in the field of sparse arrays. Numerous geometries of the DCA have been proposed, including coprime array [43, 66], nested array [42], nested subarrays [77], *etc.* DCSC geometries [32] for general MIMO active sensing along with its signal processing techniques [9] have also been studied. In HybRadar, we study the special case of "phased subarray" where the elements on each subarray form a ULA. Specifically, we have proposed the DCSC layout for phased-MIMO radar and unlike aforementioned theory-based works, we have also conducted experimental study.

9 CONCLUSION

We have presented a mmWave radar platform with a phased-MIMO architecture. The large number of antenna elements incorporated with the sparse PAM placement have led to superior angular resolution with a few RF chains. Through experimental evaluation and case studies, we have demonstrated the effectiveness of the key design choices and the versatility of HybRadar as an experimental platform. We hope the platform facilitates future research for mmWave phased-MIMO radars.

ACKNOWLEDGMENTS

We thank our shepherd and the anonymous reviewers for their insightful comments and feedback. We appreciate the thoughts and experimental assistance from Kamalakannan Subramani and Hengrui Hu. The work reported in this paper is supported in part by US Army Research Office/Department of Defense award number W911NF2020267, and by the NSF under Grants CNS-2312715, CNS-2128588, CNS-1901048, CNS-1925767.

REFERENCES

[1] Airfide Networks. 2018. Airfide Networks, a 5G company. https://airfidenet.com/.

[2] Mostafa Alizadeh, George Shaker, João Carlos Martins De Almeida, Plinio Pelegrini Morita, and Safeddin Safavi-Naeini. 2019. Remote monitoring of human vital signs using mm-wave FMCW radar. *IEEE Access* 7 (2019), 54958–54968.

[3] Analog Devices. 2014. Direct Modulation/Fast Waveform Generating, 13 GHz, Fractional-N Frequency Synthesizer. https://www.analog.com/en/products/adf4159.html#product-overview

[4] Analog Devices. 2014. Wideband VCO SMT w/Buffer Amplifier, 5 - 10 GHz. https://www.analog.com/en/products/hmc587.html#product-overview

[5] Analog Devices. 2014. x2 Active Multiplier SMT, 13 - 24.6 GHz Fout. https://www.analog.com/en/products/hmc814lc3b.html#product-overview

[6] Analog Devices. 2019. HMC8191 6 GHz to 26.5 GHz Wideband I/Q Mixer. https://www.analog.com/en/products/hmc8191.html?doc=HMC8191.pdf#product-overview

[7] Donald E Barrick. 1973. *FM/CW radar signals and digital processing*. US Department of Commerce, National Oceanic and Atmospheric Administration ....

[8] Francesco Belfiori, Wim Van Rossum, and Peter Hoogeboom. 2012. Array calibration technique for a coherent MIMO radar. In *2012 13th International Radar Symposium*. IEEE, New York, NY, USA, 122–125.

[9] Elie BouDaher, Fauzia Ahmad, and Moeness G Amin. 2015. Sparsity-based direction finding of coherent and uncorrelated targets using active nonuniform arrays. *IEEE Signal Processing Letters* 22, 10 (2015), 1628–1632.

[10] Zhang Chen, Hao Wu, and Yongxiang Liu. 2020. A novel ULA-difference-coarray-based DOA estimation method for general coherent signals. *Mathematical Problems in Engineering* 2020 (2020), 1–13.

[11] Tzu-Hsuan Chou, Nicolò Michelusi, David J Love, and James V Krogmeier. 2021. Wideband Millimeter-Wave Massive MIMO Channel Training via Compressed Sensing. In *IEEE Global Communications Conference*. IEEE, New York, NY, USA, 1–6.

[12] David L Donoho. 2006. Compressed sensing. *IEEE Transactions on Information Theory* 52, 4 (April 2006), 1289–1306.

[13] Julio Martin Duarte-Carvajalino and Guillermo Sapiro. 2009. Learning to Sense Sparse Signals: Simultaneous Sensing Matrix and Sparsifying Dictionary Optimization. *IEEE Transactions on Image Processing* 18, 7 (July 2009), 1395–1408.

[14] Ettus Research LLC. 2024. Universal Software Radio Peripheral (USRP). http://www.ettus.com/.

[15] Fortune business insights. 2022. Millimeter Wave Radar Market Size, Share & COVID-19 Impact Analysis By Vehicle Type, By Technology, By Frequency Band, and Regional Forecast, 2021-2028. https://www.fortunebusinessinsights.com/millimeter-wave-radar-market-105482.

[16] Xiaochun Ge, Wenqian Shen, Chengwen Xing, Lian Zhao, and Jianping An. 2022. Training beam design for channel estimation in hybrid mmWave MIMO systems. *IEEE Transactions on Wireless Communications* 21, 9 (2022), 7121–7134.

[17] Jian Gong, Xinyu Zhang, Kaixin Lin, Ju Ren, Yaoxue Zhang, and Wenxun Qiu. 2021. RF vital sign sensing under free body movement. *Proceedings of the ACM on Interactive, Mobile, Wearable and Ubiquitous Technologies* 5, 3 (2021).

[18] Unsoo Ha, Salah Assana, and Fadel Adib. 2020. Contactless seismocardiography via deep learning radars. In *Proceedings of the 26th Annual International Conference on Mobile Computing and Networking*. ACM, New York, NY, USA, 1–14.

[19] Kawon Han and Songcheol Hong. 2022. High-resolution phased-subarray MIMO radar with grating lobe cancellation technique. *IEEE Transactions on Microwave Theory and Techniques* 70, 5 (2022), 2775–2785.

[20] Jürgen Hasch, Eray Topak, Raik Schnabel, Thomas Zwick, Robert Weigel, and Christian Waldschmidt. 2012. Millimeter-wave technology for automotive radar sensors in the 77 GHz frequency band. *IEEE transactions on microwave theory and techniques* 60, 3 (2012), 845–860.

[21] Md Nadeem Akhtar Hasid, Subhankar Shome, Manisha Kumari Gupta, Bansibadan Maji, and Rabindranath Bera. 2020. Phased MIMO Radar Simulation for Moving Object Detection. In *Advances in Communication, Devices and Networking: Proceedings of ICCDN 2019 3*. Springer, 479–487.

[22] Aboulnasr Hassanien and Sergiy A Vorobyov. 2010. Phased-MIMO radar: A tradeoff between phased-array and MIMO radars. *IEEE Transactions on Signal Processing* 58, 6 (2010), 3137–3151.

[23] A Hedayat and Walter Dennis Wallis. 1978. Hadamard matrices and their applications. *The Annals of Statistics* 6, 6 (Nov. 1978), 1184–1238.

[24] Jeffrey S Herd and M David Conway. 2015. The evolution to modern phased array architectures. *Proc. IEEE* 104, 3 (2015), 519–529.

[25] Ralph T Hoctor and Saleem A Kassam. 1990. The unifying role of the coarray in aperture synthesis for coherent and incoherent imaging. *Proc. IEEE* 78, 4 (1990), 735–752.

[26] Jessi E Johnson, Oliver Shay, Chris Kim, and Catherine Liao. 2019. Wearable millimeter-wave device for contactless measurement of arterial pulses. *IEEE transactions on biomedical circuits and systems* 13, 6 (2019), 1525–1534.

[27] Malong Ke, Zhen Gao, Yongpeng Wu, Xiqi Gao, and Robert Schober. 2020. Compressive sensing-based adaptive active user detection and channel estimation: Massive access meets massive MIMO. *IEEE Transactions on Signal Processing* 68 (2020), 764–779.

[28] Erfan Khordad, Iain B Collings, Stephen V Hanly, and Giuseppe Caire. 2022. Compressive Sensing-Based Beam Alignment Schemes for Time-Varying Millimeter-Wave Channels. *IEEE Transactions on Wireless Communications* 22, 3 (2022).

[29] Junho Lee, Gye-Tae Gil, and Yong H Lee. 2016. Channel estimation via orthogonal matching pursuit for hybrid MIMO systems in millimeter wave communications. *IEEE Transactions on Communications* 64, 6 (June 2016), 2370–2386.

[30] Jaime Lien, Nicholas Gillian, M Emre Karagozler, Patrick Amihood, Carsten Schwesig, Erik Olson, Hakim Raja, and Ivan Poupyrev. 2016. Soli: Ubiquitous gesture sensing with millimeter wave radar. *ACM Transactions on Graphics (TOG)* 35, 4 (2016), 1–19.

[31] Darel A Linebarger, Ivan Hal Sudborough, and Ioannis G Tollis. 1993. Difference bases and sparse sensor arrays. *IEEE Transactions on Information Theory* 39, 2 (1993), 716–721.

[32] Jianyan Liu, Yanmei Zhang, Weijiang Wang, and Yilong Lu. 2016. Generalized design method for the difference co-array of the sum co-array. In *2016 IEEE International Conference on Digital Signal Processing (DSP)*. IEEE, New York, NY, USA, 385–387.

[33] M-Cube Project Website. 2024. M-Cube mmWave Software Radio. http://m3.ucsd.edu/sdr/.

[34] Minicircuits. 2017. 2 Ways MMIC Power Splitter, DC - 18000 MHz, 50Ω. https://www.minicircuits.com/WebStore/dashboard.html?model=EP2RKU%2B

[35] Minicircuits. 2017. Reflectionless High Pass Filter, 13900 - 19000 MHz. https://www.minicircuits.com/WebStore/dashboard.html?model=XHF-143M%2B

[36] Minicircuits. 2017. SMT Gain Block, 5000 - 18000 MHz, 50Ω. https://www.minicircuits.com/WebStore/dashboard.html?model=AVA-183A%2B

[37] MiniCircuits. 2018. Power Splitter/Combiner EP4RKU+ Datasheet. https://www.minicircuits.com/pdfs/EP4RKU+.pdf.

[38] Andreas F Molisch, Vishnu V Ratnam, Shengqian Han, Zheda Li, Sinh Le Hong Nguyen, Linsheng Li, and Katsuyuki Haneda. 2017. Hybrid beamforming for massive MIMO: A survey. *IEEE Communications magazine* 55, 9 (2017), 134–141.

[39] Nitin Jonathan Myers, Amine Mezghani, and Robert W Heath. 2019. FALP: Fast beam alignment in mmWave systems with low-resolution phase shifters. *IEEE Transactions on Communications* 67, 12 (Dec. 2019), 8739–8753.

[40] John Nolan, Kun Qian, and Xinyu Zhang. 2021. RoS: passive smart surface for roadside-to-vehicle communication. In *Proceedings of ACM SIGCOMM*. ACM, New York, NY, USA, 165–178.

[41] NXP. 2018. TEF82XX Customer Application Board + S32R294 Radar Application Development Board. https://www.nxp.com/products/radio-frequency/radar-transceivers-and-socs/tef82xx-customer-application-board-plus-s32r294-radar-application-development-board:TEF82-R294-KIT.

[42] Piya Pal and Palghat P Vaidyanathan. 2010. Nested arrays: A novel approach to array processing with enhanced degrees of freedom. *IEEE Transactions on Signal Processing* 58, 8 (2010), 4167–4181.

[43] Piya Pal and Palghat P Vaidyanathan. 2011. Coprime sampling and the MUSIC algorithm. In *2011 Digital signal processing and signal processing education meeting (DSP/SPE)*. IEEE, New York, NY, USA, 289–294.

[44] S Unnikrishna Pillai, Yeheskel Bar-Ness, and Fred Haber. 1985. A new approach to array geometry for improved spatial spectrum estimation. *Proc. IEEE* 73, 10 (1985), 1522–1524.

[45] Kun Qian, Zhaoyuan He, and Xinyu Zhang. 2020. 3D point cloud generation with millimeter-wave radar. *Proceedings of the ACM on Interactive, Mobile, Wearable and Ubiquitous Technologies* 4, 4 (2020), 1–23.

[46] Kun Qian, Shilin Zhu, Xinyu Zhang, and Li Erran Li. 2021. Robust multimodal vehicle detection in foggy weather using complementary lidar and radar signals. In *Proceedings of the IEEE/CVF Conference on Computer Vision and Pattern Recognition*. 444–453.

[47] Karthik Ramasubramanian. 2017. Using a complex-baseband architecture in FMCW radar systems. https://www.ti.com/lit/wp/spyy007/spyy007.pdf.

[48] Theodore S Rappaport. 2024. *Wireless communications: principles and practice*. Cambridge University Press.

[49] Frank C Robey, Scott Coutts, Dennis Weikle, Jeffrey C McHarg, and Kevin Cuomo. 2004. MIMO radar theory and experimental results. In *The 38th Asilomar Conference on Signals, Systems and Computer*, Vol. 1. IEEE, New York, NY, USA, 300–304.

[50] Swetank Kumar Saha, Yasaman Ghasempour, Muhammad Kumail Haider, Tariq Siddiqui, Paulo De Melo, Neerad Somanchi, Luke Zakrajsek, Arjun Singh, Owen Torres, Daniel Uvaydov, et al. 2017. X60: A programmable testbed for wideband 60 GHz WLANs with phased arrays. In *Proceedings of the 11th Workshop on Wireless Network Testbeds, Experimental evaluation & CHaracterization (WiNTECH '17)*. ACM, New York, NY, USA, 75–82.

[51] Ralph Schmidt. 1986. Multiple Emitter Location and Signal Parameter Estimation. *IEEE Transactions on Antennas and Propagation* 34, 3 (1986), 276–280.

[52] Dominik Schwarz, Christian Meyer, André Dürr, Ahmad Mushtaq, Wolfgang Winkler, and Christian Waldschmidt. 2021. System Performance of a Scalable 79 GHz Imaging MIMO Radar With Injection-Locked LO Feedthrough. *IEEE Journal of Microwaves* 1, 4 (2021), 941–949. https://doi.org/10.1109/JMW.2021.3100765

[53] Saeid Sedighi, Bhavani Shankar, Kumar Vijay Mishra, and Björn Ottersten. 2019. Optimum design for sparse FDA-MIMO automotive radar. In *2019 53rd Asilomar Conference on Signals, Systems, and Computers*. IEEE, New York, NY, USA.

[54] Tie-Jun Shan, Mati Wax, and Thomas Kailath. 1985. On spatial smoothing for direction-of-arrival estimation of coherent signals. *IEEE Transactions on Acoustics, Speech, and Signal Processing* 33, 4 (1985), 806–811.

[55] Zhenguo Shi, Tao Gu, Yu Zhang, and Xi Zhang. 2022. mmBP: Contact-free millimetre-wave radar based approach to blood pressure measurement. In *Proceedings of the 20th ACM Conference on Embedded Networked Sensor Systems*. 667–681.

[56] Merrill Ivan Skolnik et al. 1980. Introduction to radar systems. 3 (1980).

[57] William Sloane, Camillo Gentile, Mansoor Shafi, Jelena Senic, Philippa A Martin, and Graeme K Woodward. 2022. Measurement-Based Analysis of Millimeter-Wave Channel Sparsity. *IEEE Antennas and Wireless Propagation Letters* 22, 4 (2022), 784–788.

[58] Texas Instruments. 2015. 2.4 GHz Dual Programmable Differential Amplifier with Gain Control. https://www.ti.com/product/LMH6882

[59] Texas Instruments. 2017. Programming Chirp Parameters in TI Radar Devices (Rev. A). https://www.ti.com/lit/an/swra553a/swra553a.pdf.

[60] Texas Instruments. 2018. Imaging Radar Using Cascaded mmWave Sensor Reference Design. https://www.ti.com/lit/ug/tiduen5a/tiduen5a.pdf.

[61] Texas Instruments. 2018. single-chip 76-GHz to 81-GHz automotive radar sensor evaluation module. https://www.ti.com/tool/AWR1642BOOST.

[62] Texas Instruments. 2020. Design Guide: TIDEP-01012 Imaging Radar Using Cascaded mmWave Sensor Reference Design. https://www.ti.com/lit/ug/tiduen5a/tiduen5a.pdf.

[63] Texas Instruments. 2024. 20-GHz wideband RF synthesizer with phase synchronization & JESD204B support. https://www.ti.com/product/LMX2595

[64] Michael E Tipping. 2001. Sparse Bayesian learning and the relevance vector machine. *Journal of Machine Learning Research* 1 (June 2001), 211–244.

[65] Joel A Tropp and Anna C Gilbert. 2007. Signal recovery from random measurements via orthogonal matching pursuit. *IEEE Transactions on Information Theory* 53, 12 (Dec. 2007), 4655–4666.

[66] PP Vaidyanathan and Piya Pal. 2010. Sparse sensing with coprime arrays. In *The 44th Asilomar Conference on Signals, Systems and Computers*. IEEE, New York, NY, USA, 1405–1409.

[67] Vayyar Inc. 2019. VTRIG-74: 3D Millimeter Wave Imaging Kit. https://www.minicircuits.com/WebStore/vtrig_74.html.

[68] Christian Waldschmidt, Juergen Hasch, and Wolfgang Menzel. 2021. Automotive radar—From first efforts to future systems. *IEEE Journal of Microwaves* 1, 1 (2021), 135–148.

[69] Hongyi Wang and KJ Ray Liu. 1998. 2-D spatial smoothing for multipath coherent signal separation. *IEEE Trans. Aerospace Electron. Systems* 34, 2 (1998), 391–405.

[70] Ying Wang, Lisi Jiang, and Yongce Chen. 2015. Kronecker product-based codebook design and optimisation for correlated 3D channels. *Transactions on Emerging Telecommunications Technologies* 26, 11 (2015), 1225–1234.

[71] Yuyang Wang, Nitin Jonathan Myers, Nuria González-Prelcic, and Robert W Heath. 2021. Site-specific online compressive beam codebook learning in mmWave vehicular communication. *IEEE Transactions on Wireless Communications* 20, 5 (2021).

[72] David P Wipf and Bhaskar D Rao. 2004. Sparse Bayesian learning for basis selection. *IEEE Transactions on Signal Processing* 52, 8 (Aug. 2004), 2153–2164.

[73] Xilinx. 2023. UltraScale+ RFSoC. https://www.xilinx.com/products/silicon-devices/soc/rfsoc.html.

[74] Xilinx. 2023. ZCU111 Evaluation Board User Guide (UG1271). https://docs.xilinx.com/r/en-US/ug1271-zcu111-eval-bd/HW-FMC-XM500

[75] Zhaoyi Xu, Cong Shi, Tianfang Zhang, Shuping Li, Yichao Yuan, Chung-Tse Michael Wu, Yingying Chen, and Athina Petropulu. 2022. Simultaneous monitoring of multiple people's vital sign leveraging a single phased-MIMO radar. *IEEE Journal of Electromagnetics, RF and Microwaves in Medicine and Biology* 6, 3 (2022).

[76] Du Yang, L-L Yang, and Lajos Hanzo. 2010. DFT-based beamforming weight-vector codebook design for spatially correlated channels in the unitary precoding aided multiuser downlink. In *2010 IEEE International Conference on Communications*. IEEE, 1–5.

[77] Minglei Yang, Alexander M Haimovich, Xin Yuan, Lei Sun, and Baixiao Chen. 2018. A unified array geometry composed of multiple identical subarrays with hole-free difference coarrays for underdetermined DOA estimation. *IEEE Access* 6 (2018), 14238–14254.

[78] You You, Wuqiong Zhao, Li Zhang, Xiaohu You, and Chuan Zhang. 2023. Beam Pattern and Reflection Pattern Design for Channel Estimation in RIS-Assisted Mmwave MIMO Systems. *IEEE Transactions on Vehicular Technology* (2023).

[79] Feng Zhang, Chenshu Wu, Beibei Wang, and KJ Ray Liu. 2020. mmEye: Super-resolution millimeter wave imaging. *IEEE Internet of Things Journal* 8, 8 (2020), 6995–7008.

[80] Jialiang Zhang, Xinyu Zhang, Pushkar Kulkarni, and Parameswaran Ramanathan. 2016. OpenMili: A 60 GHz software radio platform with a reconfigurable phased-array antenna. In *Proceedings of the 22nd Annual International Conference on Mobile Computing and Networking (MobiCom '16)*. ACM, New York, NY, USA, 162–175.

[81] Yu Zhang, Ling Huang, and Jian Song. 2016. Phased array radar based angular domain channel estimation scheme for integrated radar-communication system. In *MILCOM 2016-2016 IEEE Military Communications Conference*. IEEE, New York, NY, USA, 906–911.

[82] Renjie Zhao, Timothy Woodford, Teng Wei, Kun Qian, and Xinyu Zhang. 2020. M-cube: A millimeter-wave massive MIMO software radio. In *Proceedings of the 26th Annual International Conference on Mobile Computing and Networking*. ACM, New York, NY, USA, 1–14.

[83] Kai Zheng, Aditya Dhananjay, Marco Mezzavilla, Arjuna Madanayake, Shubhendu Bharadwaj, Viduneth Ariyarathna, Abhimanyu Gosain, Tommaso Melodia, Francesco Restuccia, Josep Jornet, et al. 2019. Software-defined radios to accelerate mmWave wireless innovation. In *2019 IEEE International Symposium on Dynamic Spectrum Access Networks (DySPAN)*. IEEE, 1–4. https://doi.org/10.1109/DySPAN.2019.8935877

[84] Kai Zheng, Kun Qian, Timothy Woodford, and Xinyu Zhang. 2024. NeuroRadar: A Neuromorphic Radar Sensor for Low-Power IoT Systems. In *Proceedings of the 21st ACM Conference on Embedded Networked Sensor Systems* (Istanbul, Turkiye) *(SenSys '23)*. Association for Computing Machinery, New York, NY, USA, 223–236. https://doi.org/10.1145/3625687.3625788